Profiles of fast ions that are accelerated by high harmonic fast waves in the National Spherical Torus Experiment

D Liu[1,4], W W Heidbrink[1], M Podestà[1], R E Bell[2], E D Fredrickson[2], S S Medley[2], R W Harvey[3] and E Ruskov[1]

[1] Department of Physics and Astronomy, University of California, Irvine, CA 92617, USA
[2] Princeton Plasma Physics Laboratory, Princeton, NJ 08543, USA
[3] CompX, Del Mar, CA 92014, USA

Abstract

Combined neutral beam injection and high-harmonic fast-wave (HHFW) heating accelerate deuterium fast ions in the National Spherical Torus Experiment (NSTX). With 1.1 MW of HHFW power, the neutron emission rate is about three times larger than in the comparison discharge without HHFW heating. Acceleration of fast ions above the beam injection energy is evident on an $E||B$ type neutral particle analyzer (NPA), a 4-chord solid state neutral particle analyzer (SSNPA) array and a 16-channel fast-ion D-alpha (FIDA) diagnostic. The accelerated fast ions observed by the NPA and SSNPA diagnostics mainly come from passive charge exchange reactions at the edge due to the NPA/SSNPA localization in phase space. The spatial profile of accelerated fast ions that is measured by the FIDA diagnostic is much broader than in conventional tokamaks because of the multiple resonance layers and large orbits in NSTX. The fast-ion distribution function calculated by the CQL3D Fokker–Planck code differs from the measured spatial profile, presumably because the current version of CQL3D uses a zero-banana-width model. In addition, compressional Alfven eigenmode activity is stronger during the HHFW heating and it may affect the fast-ion spatial profile.

(Some figures in this article are in colour only in the electronic version)

1. Introduction and motivation

Neutral beam injection (NBI) and high harmonic fast wave (HHFW) are the two major auxiliary heating systems in the National Spherical Torus Experiment (NSTX) [1]. Up to 7.5 MW of NBI

[4] Present address: Department of Physics, University of Wisconsin-Madison, Madison, WI 53706, USA.

power and 6 MW of HHFW power can be deposited into bulk deuterium plasmas in NSTX [2]. The interactions between fast waves and fast ions from NBI have been extensively studied in many toroidal fusion devices [3]. The wave absorption by fast ions at the fundamental cyclotron frequency or low harmonics can form an energetic, anisotropic tail distribution and this wave absorption competes with electron absorption, which reduces the available power for electron heating and current drive by the fast waves. Acceleration of fast ions at the third, fourth and fifth harmonics is now an established technique and has been demonstrated in many recent experiments [4–15]. In particular, the $k_\perp \rho_f$ dependence ($k_\perp$ is the perpendicular wavenumber and ρ_f is the fast-ion gyroradius) is well established. The discharges in NSTX provide a unique opportunity for studying the interactions between HHFW and fast ions at high β and dielectric constant. Because of the relatively low magnetic field, fast ions produced during NBI in NSTX are super-Alfvenic and the ratio of the gyroradius to the perpendicular wavelength is very large. In addition, the spacing between harmonic layers is much narrower than in conventional aspect-ratio tokamaks especially when compared with orbit size. Significant absorption of HHFW power at multiple cyclotron harmonics is expected. These differences of NSTX from conventional tokamaks motivate this careful comparison between theory and experiment in this unusual regime.

The acceleration of fast ions by HHFW in NSTX was previously studied by Rosenberg *et al* with neutron and $E||B$ type neutral particle analyzer (NPA) measurements [14]. Although the acceleration was observed by both diagnostics, little information was obtained on the spatial profile of the absorption. With the installation of the NSTX fast-ion D-alpha (FIDA) diagnostic [16–18], radially resolved measurements of the fast-ion profile are now possible. FIDA measurements of accelerated beam ions by high harmonic cyclotron heating in DIII-D were recently published [15].

The outline of this paper is as follows. The experimental conditions and main fast-ion diagnostics in NSTX are described in section 2. A complete description of the newly developed FIDA diagnostic is available in [18]. Experimental measurements from neutron detectors, the $E||B$ type NPA, solid state neutral particle analyzer (SSNPA) and FIDA diagnostics are presented in section 3. The measurements clearly show that fast ions are accelerated by HHFW heating. The spatial profile of FIDA measurements also shows the difference between fast wave heating in NSTX and in conventional toroidal devices (section 3.3). Section 4 discusses the observations and compares the measurements with simulation results from the Fokker–Planck code CQL3D [19]. The paper concludes with a summary in section 5.

2. Experimental conditions and major fast-ion diagnostics

The data in this paper are from a half day run during the 2008 experimental campaign. During 2008, NSTX (a small aspect-ratio spherical torus, with major and minor radius of $R_0 \simeq 0.85$ m and $a \simeq 0.67$ m) was equipped with three co-injected neutral beam (NB) sources with tangency radii of 0.69 m (source A), 0.59 m (source B) and 0.49 m (source C) and a HHFW heating system in a full 12-antenna, 6-transmitter configuration. In our experiment, NB source B is modulated in order to minimize fast-ion driven instability and perform background subtraction for fast-ion diagnostics.

The major fast-ion diagnostics on NSTX include neutron detectors, an $E||B$ type NPA [20, 21], a 4-chord SSNPA array [22, 23] and a 16 channel FIDA diagnostic [16–18] (figure 1(*a*)). The neutron detectors on NSTX consist of both ^{235}U fission chambers and plastic scintillators. They give an absolutely calibrated measure of the volume-averaged 2.5 MeV neutron rate R_n from D–D fusion reactions between beam ions and bulk plasma ions. (The beam–plasma reaction rate is over one order of magnitude larger than the beam–beam or
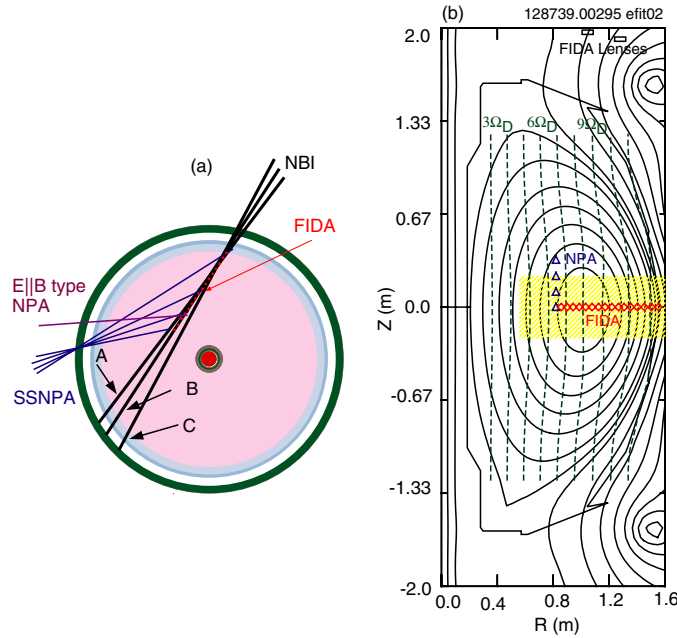
Figure 1. (*a*) Midplane view of the NSTX showing the three co-injected neutral beam sources, *E*||*B* type NPA, SSNPA array and midplane locations of the FIDA channels. (*b*) Elevation of the NSTX vacuum vessel, showing the flux surfaces (solid curves), the locations where ω_{RF} equals the 3rd–11th deuterium cyclotron harmonics (dashed lines), the midplane locations of the FIDA channels (diamonds) and elevation minor radii of the *E*||*B* type NPA during the four-shot vertical scan (triangles). The hatched region represents the approximate extent of the neutral beam that produces the FIDA and NPA signals. The rectangles indicate the approximate locations of the FIDA lenses.

thermonuclear rate.) The neutron emission rate R_n depends strongly on the density of high energy, centrally confined fast ions due to the energy dependence of the fusion cross-section and to the higher density of target ions in the plasma core. Both the *E*||*B* type NPA and SSNPA diagnostics measure fast ions that charge exchange (CX) with injected beam neutrals or background neutrals. (CX reactions between fast ions and injected beam neutrals are called active CX, while passive CX reactions happen between fast ions and background neutrals.) The *E*||*B* type NPA on NSTX utilizes a PPPL-designed *E*||*B* spectrometer which measures the energy spectra of H and D simultaneously with 39 energy channels per mass species and a time resolution of 1 ms. The *E*||*B* type NPA is capable of both horizontal and vertical scanning on a shot-to-shot basis. The SSNPA array on NSTX consists of four chords with fixed tangency radii of 60, 90, 100 and 120 cm in the midplane. Each chord utilizes a silicon photodiode that is coupled to a fast digitizer to measure the energy distribution of CX fast neutral particles (30–100 keV). The energy resolution is about 10 keV and the time resolution is 2 ms. The FIDA diagnostic is a charge exchange recombination spectroscopy measurement that exploits the large Doppler shift of Balmer-alpha light from energetic hydrogenic atoms to infer the fast-ion density. The techniques of beam modulation and fitting of impurity lines are often used to extract the fast-ion spectra from the interfering background light [24, 25]. Since the photon Doppler shift is determined by one component of the velocity, energy E_λ (converted from light wavelength) is the energy component of fast ions along the viewing channel (which is almost vertical in our setup), not the total energy. The FIDA diagnostic

3

performs an effective average in velocity space over this and higher energies. Since the FIDA signals are proportional to the product of injected neutral density and the fast-ion density, the wavelength-integrated (or energy-integrated) FIDA signals are usually divided by the injected neutral density (as calculated by a pencil-beam code) to obtain FIDA density [18] measurements over the high-energy portion of velocity space. The spatial and spectral resolutions of the FIDA diagnostic are 5 cm and 10 keV and the time resolution is 10 ms. All the FIDA data used in this paper are from the 16 active channels with background subtraction obtained through beam modulation. The measured signals from the line-integrated NPA and FIDA diagnostics are mainly core-weighted due to active CX reactions with beam neutrals in the intersectional area. However, under certain conditions, the signals from the NPA diagnostics can be edge-weighted due to passive CX reactions with wall neutrals. Plasma profiles are measured by multipoint Thompson scattering system [26] and charge exchange recombination spectroscopy system [27]. Magnetic field fluctuations are measured by Mirnov coils that are located close to the vacuum vessel wall at the low-field side.

The RF frequency of the antenna in NSTX is 30 MHz and the fast wave is launched counter-directed relative to the pre-existing plasma current with parallel wavenumber $k_{\parallel}$ of $8\,m^{-1}$ and the phase difference between adjacent antenna straps of $90°$. Although the HHFW power couples predominantly to the electrons, the power absorbed by fast ions could take more than 30% of the total input HHFW power [14]. At the usual toroidal field of 0.55 T, the 30 MHz waves resonate with deuterium cyclotron harmonics at several radial locations with the central resonance corresponding to the eighth harmonic and the outer edge resonance corresponding to the eleventh harmonic, as shown in figure 1(*b*). In all the shots presented in this paper, the toroidal magnetic field is about 0.55 T at the magnetic axis, the plasma current is about 800 kA, the outer gap is about 3–4 cm, and the central density is around $3.0 \times 10^{13}\,cm^{-3}$.

3. Experimental results

The temporal evolution of plasma parameters in typical discharges with and without HHFW heating is shown in figure 2. Neutral beam source A at 90 keV is applied at two times of 0.06–0.15 s and 0.42–057 s to obtain motional Stark effect (MSE) [28] data. During the time of 0.15–0.4 s, short pulses of neutral beam source B inject approximately 1.1 MW of ~65 keV deuterons into deuterium NSTX plasmas. The 30 MHz HHFW system couples ~1.1 MW of power between 0.21 and 0.37 s. As shown in figure 2(*b*), plasma parameters (plasma current and electron temperature) in the nominally identical RF shots and the no-RF reference shot are similar except that the electron density n_e is larger in the RF shots. With the beam modulation technique and relatively low injection energy, there is no robust MHD activity in the spectra of Mirnov signals (figure 2(*c*)). Weak compressional Alfven eigenmodes (CAEs) exist in the shots with and without HHFW heating (figure 3). However, the CAEs during the HHFW heating are about 25% stronger in mode magnitude and show some chirping feature with frequency sweep of 150 kHz. This may affect the fast-ion spatial profile.

3.1. Neutron measurements

Neutron measurements clearly show that beam ions are accelerated by HHFW heating. Since the NB is modulated, the neutron emission rate shows a similar modulation trend as the injected NB. As shown in figure 2(*d*), the time-averaged level of neutron emission rate rises by about a factor of three during the HHFW heating. Because the neutron rate is dominated by beam–plasma reactions, this indicates that a significant fraction of high-energy fast ions are accelerated by the RF heating. The pulses in the neutron rate between 0.17 and 0.37 s are
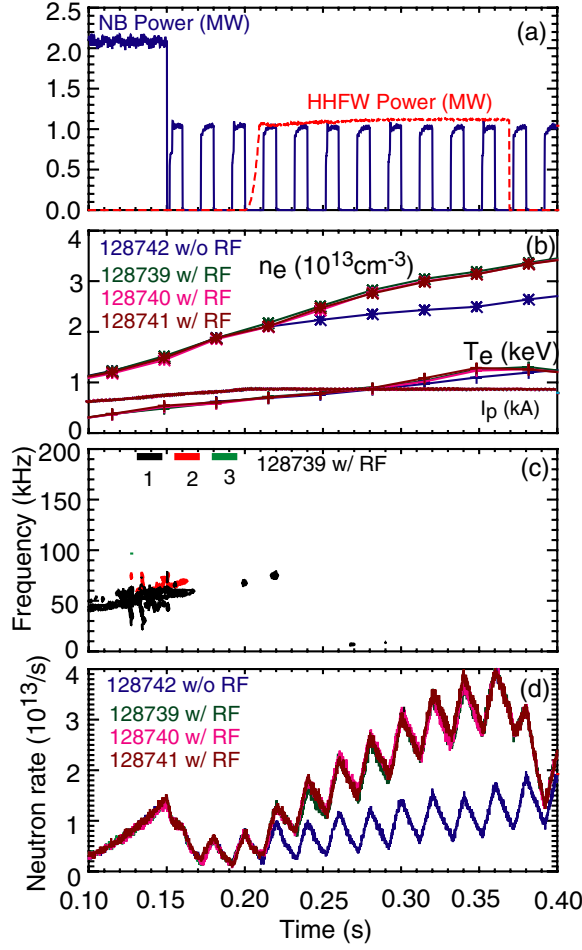
Figure 2. Temporal evolution of (*a*) injected NB power and HHFW power and (*b*) central electron density, electron temperature and plasma current in the no-RF reference shot 128742 and the three nominally identical shots 128739–128741. (*c*) Spectrum of Mirnov coils of shot 128739 in the low frequency range of [0, 200] kHz. (*d*) The d–d neutron emission rates in the no-RF reference shot 128742 and the three nominally identical shots 128739–128741.

analyzed using the technique described in [29]. For each pulse, the neutron emission R_n rises nearly linearly during the beam injection, then decays approximately exponentially following the pulse. Because the rise depends on the number of confined beam ions and the decay depends on beam ion slowing down and loss, the neutron signal can be fitted to the equation $dR_n/dt = c - R_n/\tau_n$ during the beam pulse and to $dR_n/dt = -R_n/\tau_n$ after the pulse, where the constant c reflects the prompt confinement of the injected beam ions and is proportional to $(dN_b/dt)n_d\langle\sigma v\rangle$. Here dN_b/dt is the rate at which full-energy beam ions are injected into the device, n_d is the deuterium density in the center of the device, $\langle\sigma v\rangle$ is the averaged D–D reactivity and τ_n is the neutron decay time. As shown in figure 4(*a*), the rise rate c of the neutron emission in the HHFW heating shots agrees well with that in the no-RF reference shot prior to the injection of HHFW power, but it is slightly larger upon the injection of HHFW power. This is because the deuterium density n_d is slightly larger due to the higher electron
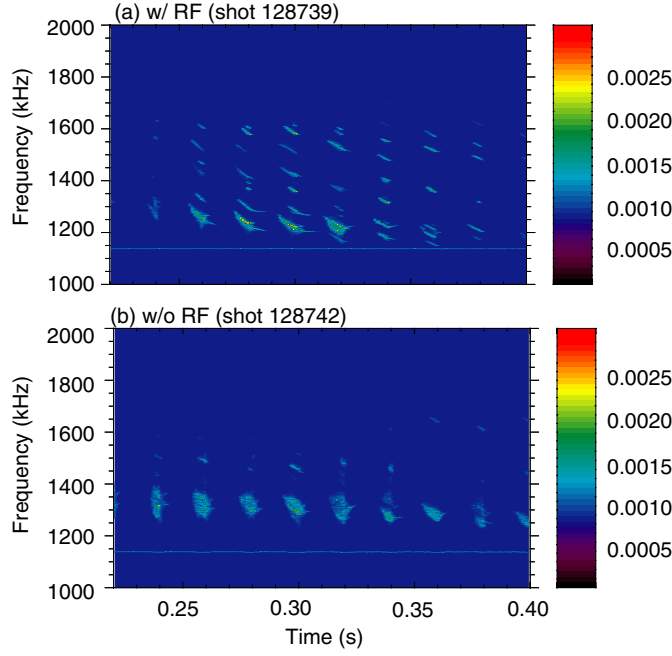
Figure 3. Spectra of Mirnov coil signals in the frequency range of [1000, 2000] kHz in the discharges with and without HHFW heating. Note that the FFT mode amplitude in our experiment is relatively weak (less than 1/4 of that in typical NSTX plasmas).

density during the HHFW heating. As shown in figure 4(*b*), the neutron decay time τ_n in the HHFW heating shots agrees well with the no-RF reference shot prior to the injection of HHFW power, but increases substantially upon injection of HHFW power. This is because the size of the tail of the distribution is determined by a competition between Coulomb drag and acceleration by cyclotron absorption. The beam ion distribution function f can be described by the Fokker–Planck equation

$$\frac{\partial f}{\partial t} = C + Q + S,$$

where C represents the collision operator, Q represents the RF operator and S represents particle sources and sinks. When the NB is turned off, $S \simeq 0$ at high energies. Then the neutron decay during the beam turn-off period reflects the competition between Coulomb deceleration and HHFW acceleration. From figure 4(*b*), it can be estimated that the high-energy ions that dominate the D–D beam-target fusion neutron rate experience strong acceleration that, on average, is nearly 0.5–0.7 of the Coulomb drag in the shots 128739–128741. The experimental data (discrete points with vertical error bars in figure 4) are also compared with the predictions (solid lines in figure 4) from the TRANSP code [30–32], which uses measured temperature, density, impurity and rotation profiles and assumes fast ions behave classically (but not including any model for HHFW-induced acceleration). The rise rate of the neutron pulses is accurately modeled by TRANSP both before and during the HHFW injection, because the beam ions that have just been injected have not had enough time to be accelerated, so they produce the same number of neutrons before and during the HWFW heating. The predicted neutron decay time is in good agreement with the measured values prior to the HHFW injection, but it is much smaller than the measurements during the HHFW heating. This indicates that
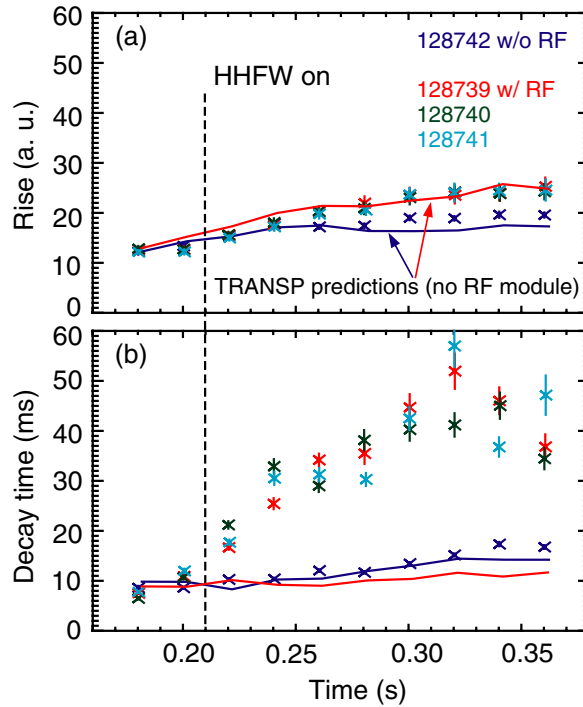
Figure 4. (*a*) Rise rate and (*b*) decay time of neutron emission rate versus time in the discharges with and without HHFW heating. The symbols represent experimentally measured values. The solid lines are TRANSP predictions that employ the measured profiles but do not take into account HHFW-induced acceleration of the beam ions.

fast ions are accelerated by the HHFW heating, which increases the slowing-down time above the classical value and consequently the fast-ion density.

3.2. NPA and SSNPA measurements

The application of HHFW gives perpendicular energy to fast ions through cyclotron resonance. In [14], a clear fast-ion tail due to HHFW heating in NSTX was observed on the $E||B$ type NPA diagnostic when HHFW and NBI were active simultaneously. Furthermore, the tail decayed to the no-RF spectrum after RF turnoff with NBI remaining active. Unfortunately, in our experiment, the NPA energy spectra are contaminated by RF-induced noise. However, with the assumption that the RF-induced noise is unaffected by the modulated NB, active CX energy spectra can be obtained by subtracting the NPA signal in the beam-off period from that in the beam-on period. In this way, the RF-induced noise and the passive CX signal are effectively removed and the measured NPA energy spectrum in the NBI only case is similar to the TRANSP prediction. As shown in figure 5, the active CX energy spectrum of the $E||B$ type NPA in the HHFW heating shot 128739 shows only a small D^+ tail above the beam injection energy. Similarly, the active CX energy spectra from the SSNPA do not show any obvious D^+ tail (not shown here), but the total energy spectra (which is the summation of active and passive CX signals) of SSNPA show a D^+ tail up to 100 keV (figure 6). (Note that the energy spectrum which shows an accelerated fast-ion tail in [14] is also the energy spectrum of the NPA total signals.) This suggests that the accelerated fast ions that are observed by the NPA diagnostics are mainly from the passive CX reactions at the edge. The reason why the active signals do
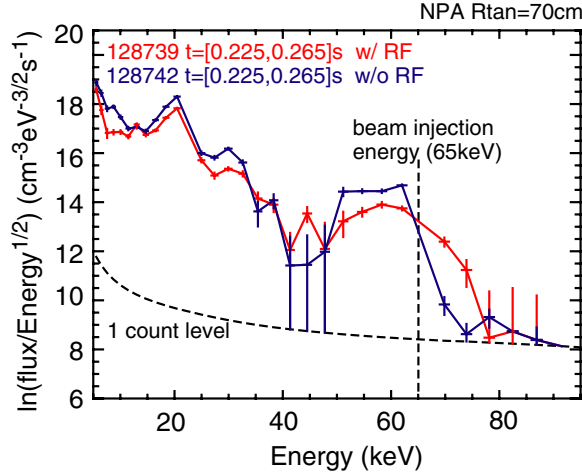
7

Figure 5. Energy spectra of active CX signals from the $E||B$ type NPA at a sightline tangency radius of 70 cm for NSTX shots 128739 (with RF) and 128742 (without RF).

not show an obvious D^+ tail is that the small portion of phase space observed by the NPA was weakly affected by the HHFW heating. More details will be presented in the discussion section. In our experiment, the $E||B$ type NPA also scanned vertically shot-to-shot so that the pitch ($p = v_{||}/v$) changes from more parallel ($p \simeq 0.8$) to more perpendicular ($p \simeq 0.72$). The active CX signals from this pitch-angle scan show fast ions are accelerated 10 keV above the injection energy (figure 7) and a strong fast-ion tail is observed at the vertical angle of $12°$ (the elevation minor radius is 33 cm). The energy spectra of total signals from the SSNPA measurements (figure 8) during these nominally identical shots show that the acceleration of fast ions is strong in the chords 1–3 whose pitches at the edge are between 0.3 and 0.5. It also suggests that the acceleration is strong in the more perpendicular direction, as expected for fast wave heating.

3.3. FIDA measurements

FIDA data also confirm that fast ions are accelerated by fast waves. Figure 9 shows the comparison of the FIDA energy spectra in the discharges with and without HHFW heating. It shows that the FIDA density, which is proportional to the local fast-ion density, of channel 11 with $R_{maj} = 108$ cm in the energy range of $E_\lambda = 15$–65 keV is much larger in the discharges with RF than without RF. For example, the FIDA density for $E_\lambda \simeq 42$ keV, which is actually dominated by the fast ions with beam injection energy and angle ($E_\lambda \simeq 65$ keV, $p \simeq 0.6$), increases by a factor of 2 in the RF shots. The data indicate that fast ions are accelerated and some of them are above the beam injection energy.

In order to determine the radial position of the fast-ion acceleration, figure 10 shows the enhancement of the energy-integrated FIDA density in the HHFW heating shots as a function of major radius. For both energy integration ranges in figure 10, the FIDA density increases significantly in the RF shots in a very broad region. The enhancement is largest between the $7\Omega_D$ and $8\Omega_D$ harmonic resonance layers. (The magnetic axis $R_{maj} \simeq 100$ cm is also in that region.) This is different from the observations in DIII-D [15]. More details will be presented in the discussion section. The peak in the FIDA density enhancement around $R_{maj} = 150$ cm occurs near the $11 \Omega_D$ harmonic resonance layer; this increase in signal is also accentuated
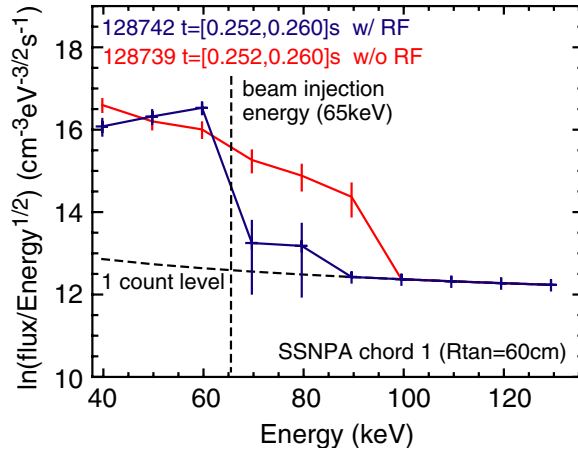
Figure 6. Energy spectra of total signals of chord 1 of SSNPA with tangency radius of 60 cm for NSTX shots 128739 (with RF) and 128742 (without RF).
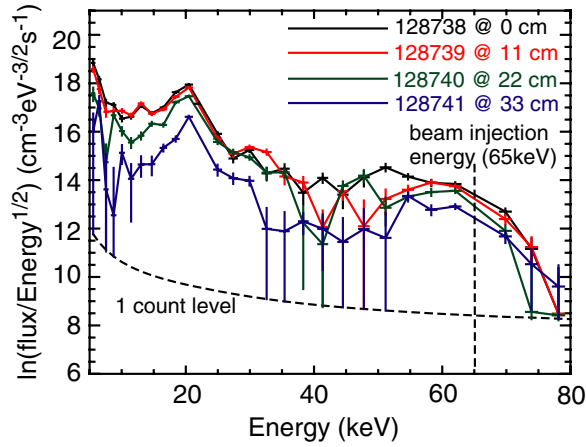

Figure 7. Energy spectra of active signals from the $E \| B$ type NPA during four nominally identical discharges, in which the NPA scanned vertically with vertical angles of $0°$, $4°$, $8°$ and $12°$ above the midplane (corresponding elevation minor radius at beam intersection of 0 cm, 11 cm, 22 cm, 33 cm, respectively). The NPA tangency radius is 70 cm.

because the channel is close to the plasma boundary where the FIDA density in the no-RF reference shot is small. Figure 10 shows that the enhancement of the FIDA density in the energy integration range of $E_\lambda = 30$–65 keV (figure 10(*b*)) is about twice as large as the FIDA density enhancement ($\sim$1.5) in the energy integration range of $E_\lambda = 10$–65 keV (figure 10(*a*)). This is because HHFW heating is a finite Larmor radius effect that depends upon the value of $k_\perp \rho_{\rm f}$. The observation is consistent with the theoretical expectation that higher energy ions should be most strongly affected.

4. Discussion and comparison with theory

As shown in section 3.2, the fast-ion tail above the beam injection energy observed by the NPA diagnostics is mainly from the passive CX reactions at the edge, not from the active
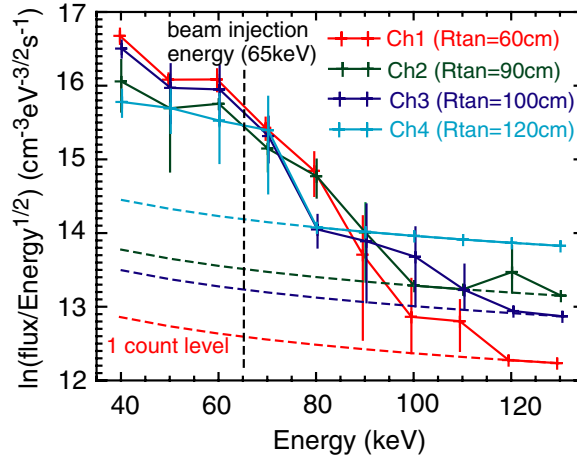
Figure 8. Averaged energy spectra of total CX signals of four chords of SSNPA in four nominally identical discharges 128738–128741 with HHFW heating. The vertical error bars are the standard deviation of SSNPA signals in these identical discharges. The acceleration of fast ions is strongest in chords 1–3 whose pitches at the edge are between 0.3 and 0.5.
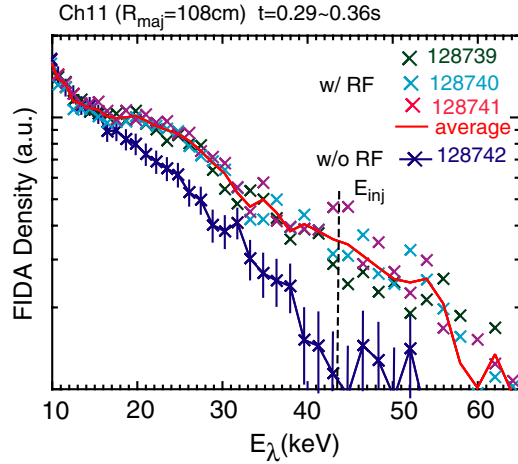

Figure 9. Energy spectra of channel 11 ($R_{\mathrm{maj}} = 108$ cm) of the FIDA diagnostic in the no-RF reference shot 128742 and three nominally identical RF shots 128739–128741 (where the upper solid line is the average of the three RF shots). The vertical error bars in shot 128742 show typical statistical error in these shots. Note that the energy axis E_λ is the energy component of fast ions along the viewing sightline. The FIDA signal for $E_\lambda = 42$ keV is actually dominated by ions born near the beam injection energy and pitch ($E_{\mathrm{inj}} \simeq 65$ keV and $p \simeq 0.6$).

CX reactions at the intersectional area. This can be understood by looking at the fast-ion distribution in velocity space. Fast ions produced by NBI are mainly confined around the magnetic axis. For the NB injection geometry, the pitch of the confined fast ions is ∼0.6, which is shown as the solid line in figure 11 with diamond symbols representing the full, half and third energy components of NB injection energy. The geometry of the NPA/SSNPA sightlines determines the pitch at which fast ions can contribute to the NPA/SSNPA active CX signals. It is ∼0.8 for the $E\|B$ type NPA at tangency radius of 70 cm and it is shown as the dash-dotted line in figure 11. For the SSNPA sightlines, the pitch range for active CX signals
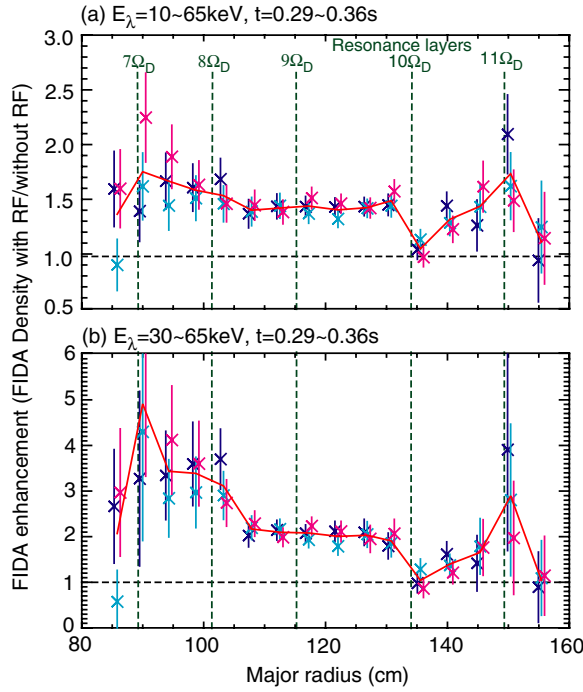
Figure 10. Relative change in integrated FIDA density in the discharges with and without HHFW heating for energy integration range of (*a*) $E_\lambda = 10$–65 keV and (*b*) $E_\lambda = 30$–65 keV during the time window of 0.29–0.35 s. The symbols represent the FIDA enhancement in three nominally identical RF shots (128739, 128740 and 128741) relative to the no-RF reference shot 128742. The solid line is the average of the three RF shots. The vertical error bars are statistical error. The vertical dashed lines are nominal resonance layers.

is 0.75–0.9 (not shown in the graph). The shaded region shows the pitch range in which fast ions can contribute to the NPA and SSNPA passive CX signals. During the HHFW heating, a fast ion gains perpendicular energy through cyclotron resonance and thus its pitch shifts upward in velocity space. For example, when a 65 keV fast ion gains 35 keV of perpendicular energy, it can move upward in the velocity space and enter the shaded region. Then it becomes detectable for the NPA/SSNPA passive CX signals. For the fast ions with pitch less than 0.8, when they gain perpendicular energy, they move farther away from the dash-dotted line and they cannot be detected by the NPA diagnostic. In addition, very few fast ions are in the region with pitch between 0.9 and 1.0 and the wave electric field at the $6\Omega_D$ harmonic is relatively small. The combination of these effects explains why the NPA diagnostics measure little fast-ion acceleration in the active CX signals but clearly observe the tail in the passive CX signals.

Since fast wave heating imparts only perpendicular energy to fast ions, it will produce fast ions with banana tips or turning points near resonance layers. (This effect has been termed resonance localization.) So the other way to understand the NPA/SSNPA observations is to trace back the trajectories of fast ions before the CX reaction. One example is shown in figure 12. The fast ion that can contribute to the SSNPA passive CX signals is a barely passing particle and the turning point is near the central resonance layers (figures 12(*a*) and (*b*)) and the fast ion spends much of its orbit at resonance layers. This is the result of gaining perpendicular energy. In figures 12(*c*) and (*d*), the fast ion that can contribute to the SSNPA active CX
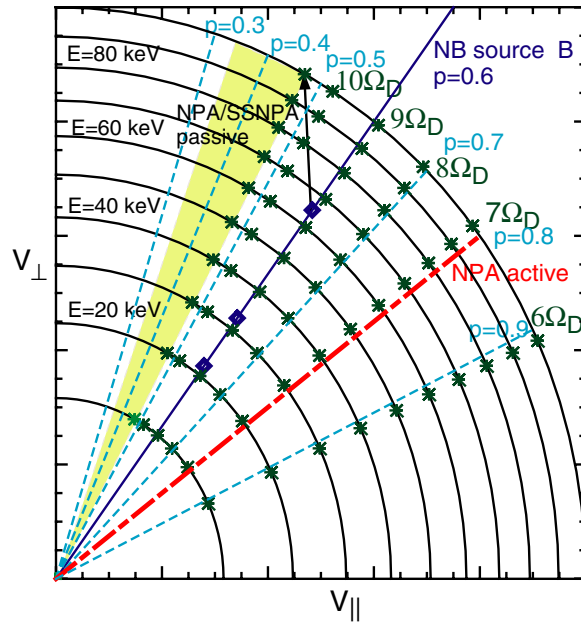
Figure 11. Velocity space of fast ions. The solid line shows the pitch of fast ions from NBI at the magnetic axis with diamond symbols representing the full, half and third energy components of the NB injection energy. The dash-dotted line shows the pitch at which fast ions can contribute to the NPA active CX signals. The pitch range for SSNPA active CX is 0.75–0.9. The shaded region shows the pitch range in which fast ions can contribute to the NPA and SSNPA passive CX signals. The symbols represent the pitches of fast ions at nominal resonance layers.

signals is a well confined passing particle. This type of particle is not produced by fast wave heating. This is consistent with our observations that the SSNPA active CX signal does not see a 100 keV fast-ion tail, but the SSNPA passive CX signal does.

The pitch of the observed orbits also explains the results of the NPA vertical scan (figure 7). The similarity between the NPA signals at vertical angles of $0°$, $4°$ and $8°$ (with elevation minor radii of 0 cm, 11 cm and 22 cm) can be understood by noting that the magnitude of NPA signals is due to the competing effects of pitch angle and neutral particle density localization. With the increase in vertical angle (or elevation minor radius), the beam neutral density is lower and the pitch becomes modestly closer to the pitch ($\sim$0.6) of the injected NB. For example, the beam neutral density at a vertical angle of $4°$ is lower than that at $0°$. But a particle at a vertical angle of $4°$ would have to pitch angle scatter less to find its way to the $E||B$ type NPA. Thus, the final NPA signals are comparable for vertical angles at $0°$ and $4°$. At the vertical angle of $12°$, the beam neutral density decreases dramatically. So the lower signal is understandable. More importantly, a fast-ion tail is seen at the vertical angle of $12°$ because the NPA is in a more perpendicular direction.

To summarize the neutral particle observations, fast ions above the beam injection energy are observed whenever the NPA/SSNPA detects pitch angles that are more perpendicular than the angle of injection.

As shown in figure 10 of section 3.3, the FIDA density is enhanced significantly in a very broad range from the $6\Omega_D$ to $10\Omega_D$ harmonic resonance layers. The enhancement region is much broader than that in the DIII-D [15] case, in which the FIDA spatial profile peaks about 8–10 cm farther out in radius than the nominal resonance layer (due to the nature of
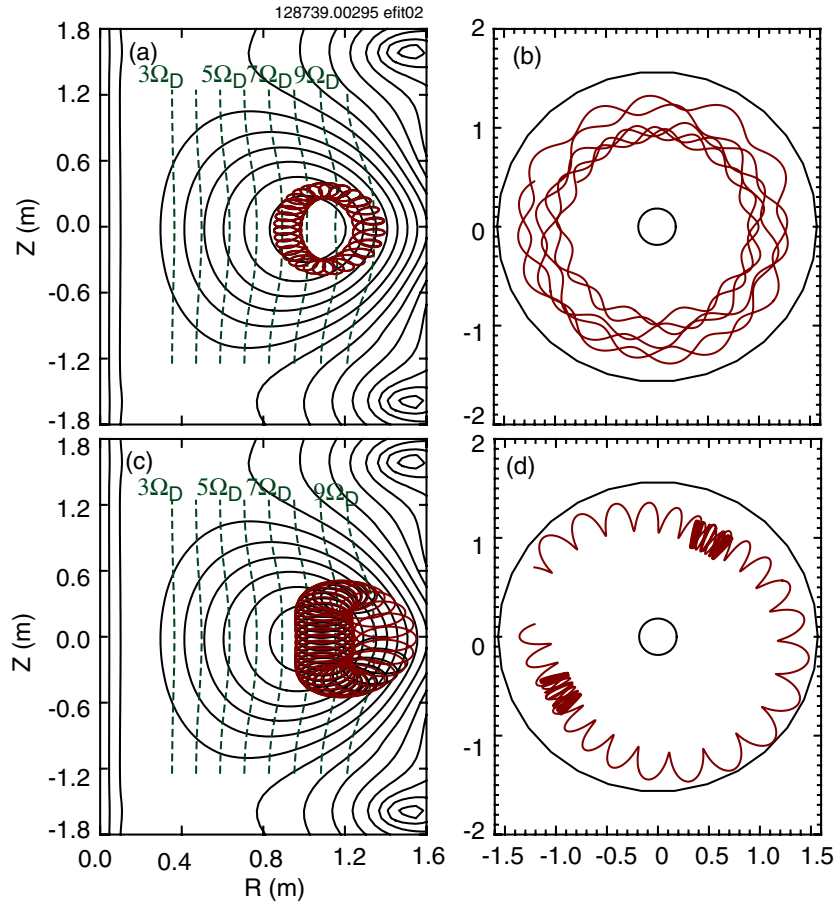
Figure 12. (*a*) Elevation and (*b*) top view of trajectory of a fast ion ($E = 100\,\text{keV}$ and pitch $= 0.8$) that can CX at $R = 0.9\,\text{m}$ and contribute to the NPA active CX signals; (*c*) elevation and (*d*) top view of trajectory of a fast ion ($E = 100\,\text{keV}$ and pitch $= 0.4$) that can CX at $R = 1.4\,\text{m}$ and contribute to the NPA passive CX signals.

banana orbits) and the full width at half maximum (FWHM) is about 15 cm. The difference can be explained by the multiple and closely spaced resonance layers in NSTX and the large gyroradius of fast ions. In NSTX, there are four or five resonance layers in typical discharges from plasma center to plasma edge as shown in figure 1(*b*). The gyroradius of the fast ions with perpendicular energy of 50 keV is about 8.3 cm at the usual NSTX toroidal magnetic field of 0.55 T. (In contrast, in DIII-D there are only one or two resonance layers and the gyroradius of the fast ions is around 2.3 cm at a toroidal magnetic field of 2 T.) In addition, the orbit drift displacement is about 20 cm (figure 12) and is comparable to the spacing between resonance layers in NSTX. The combination of these factors results in accelerated fast ions throughout the plasma cross-section, in contrast to the localized profiles observed in conventional tokamaks [33–35].

The Fokker–Planck equation for the fast-ion distribution function during HHFW heating can be solved with the CQL3D code [19] and it can be used as an input in a forward-modelling NPA and FIDA simulation code [16] to compare with measurements. In the version of the CQL3D code employed here, the fast-ion orbits are treated in a zero-banana-width
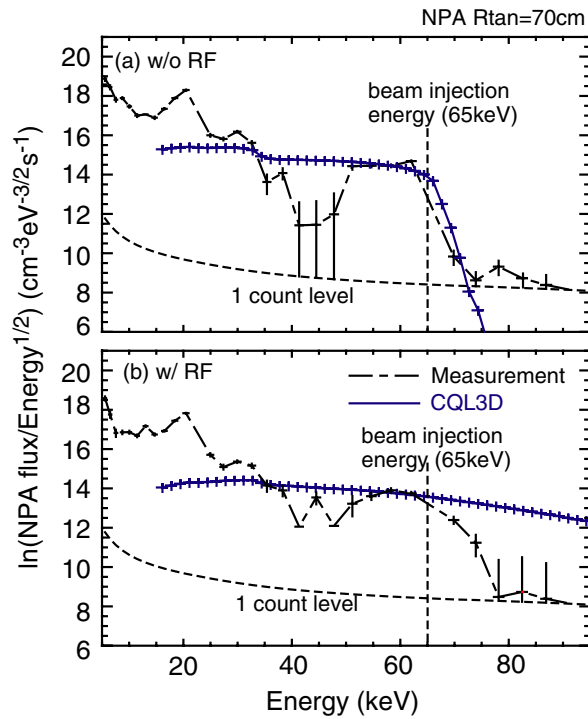
Figure 13. Comparison of measured NPA energy spectra and NPA simulations using CQL3D predicted fast-ion distributions in the shots (*a*) without and (*b*) with HHFW heating.

approximation and the wave fields in the quasilinear RF operator Q are calculated using ray tracing. Two cases are simulated with the CQL3D code. In the first case, only NBI is considered and it is similar to the no-RF reference shot 128742. The second case includes the interactions between HHFW and fast ions from NBI and it is similar to the three nominally identical RF shots. In both cases, the modulated NB in experiments is replaced with a steady beam that injects the average power. The CQL3D simulations predict a fourfold increase in the neutron emission rate with RF; the measured neutron rate increase is a factor of three. The calculated fast-ion distributions are mapped into the coordinates used in the NPA and the FIDA simulation code, namely $F(E, p, x, y, z)$, where E is the energy, p is the pitch of fast ions and (x, y, z) are Cartesian coordinates along the neutral beam that produces the NPA and FIDA signals. Then the code uses the F and the computed injected beam neutral and halo neutral densities to predict the NPA signal and FIDA spectral intensity. The FIDA simulation code has been verified in quiescent plasmas in the DIII-D tokamak [25] using the fast-ion distribution calculated by TRANSP. In the DIII-D case, the simulation gives good agreement with the measured FIDA intensity and spectral shape.

Figure 13 shows the comparison between the NPA simulations and measurements. Since there is no robust MHD instability in the no-RF reference shot (as shown in figure 2(*c*)), the simulated NPA energy spectra are expected to agree with the measurements. As shown in figure 13(*a*), the simulated magnitude roughly agrees with the measurement, but it does not show the strong drop between the NB full and half energy components. In other words, the NPA simulations predict that slowing down fast ions fill up the energy range between the full and half energy components, but this is not observed experimentally. Figure 13(*b*) shows that the NPA simulations predict that the NPA should see a fast-ion tail in the active CX signals
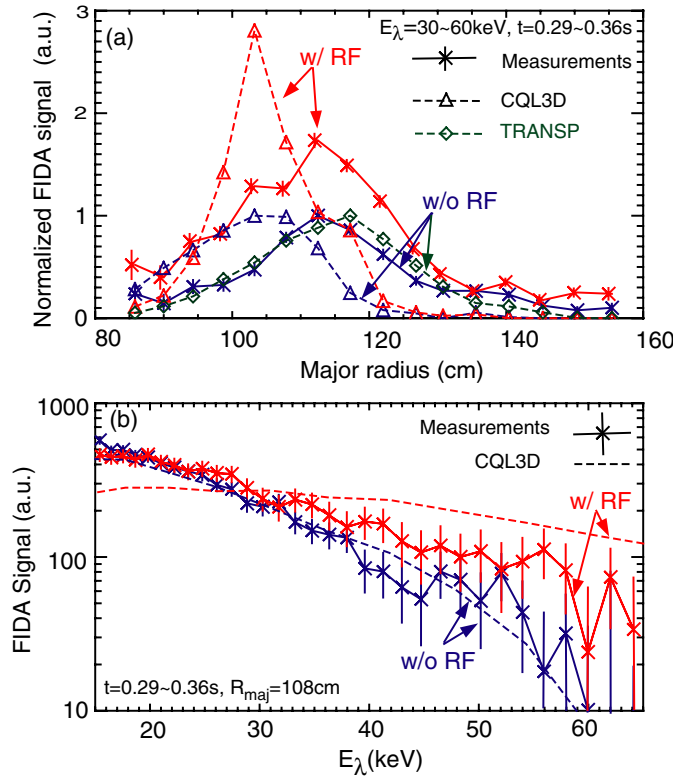
Figure 14. Comparison of (*a*) FIDA spatial profiles and (b) FIDA energy spectra of chord 11 with $R_{\mathrm{maj}} = 108$ cm from measurements and simulations using TRANSP or CQL3D predicted fast-ion distributions.

during the HHFW heating, which is also contrary to our observations. A possible reason for these discrepancies is that the input fast-ion distribution is not sufficiently accurate, especially in velocity space because of the zero-banana-width assumption in the CQL3D code and the large gyroradius of fast ions in NSTX. Note that the NPA diagnostics measure a small volume in velocity space.

The simulated FIDA spatial profiles and energy spectra are compared with the measurements in figure 14. In the no-RF reference case, the shape of the spatial profile from a FIDA simulation based on the TRANSP fast-ion distribution agrees well with the measurement. However, the FIDA simulations that use the CQL3D fast-ion distribution predict that the peak of the FIDA spatial profile is closer to the magnetic axis ($R_0 \simeq 100$ cm) and narrower than the measurements (figure 14(*a*)). During RF, the simulations predict a signal enhancement of about 3, while the measured enhancement is about 2 in the energy integration range 30–60 keV. This difference is also evident in the energy spectra (figure 14(*b*)). These discrepancies are likely due to the zero-banana-width approximation in the CQL3D simulation.

5. Conclusion

The acceleration of fast ions due to HHFW heating in NSTX is clearly observed with the neutron, $E \| B$ type NPA, SSNPA and FIDA diagnostics. With 1.1 MW of HHFW power, the

neutron rate is about three times larger than in the comparison discharge without HHFW heating. At some tangency radii, the SSNPA can detect neutrals at twice the injection beam energy. The fast-ion tail above the injection energy observed by the NPA and SSNPA diagnostics is mainly from the passive CX reactions at the edge, not from the active CX reactions in the intersectional area. For the measurement geometry, the passive NPA signals are more sensitive to the perpendicular part of phase space than the active signals. The SSNPA measurements also suggest that the acceleration of fast ions is strong in the perpendicular direction. All of these observations are consistent with theories of RF heating. The measurements by the FIDA diagnostic indicate that the acceleration is mainly in higher energy beam ions and the fast-ion density can be increased by a factor of two at the beam injection energy. The measured FIDA spatial profile of accelerated fast ions shows that the enhancement is in a much broader region than in conventional tokamaks due to the multiple and closely spaced resonance layers and large orbits in NSTX. The energy dependence of the fast-ion distribution function calculated by the CQL3D Fokker–Planck code is fairly consistent with the measurements but the predicted profile differs from the measurements. The peak of the simulated FIDA spatial profile is closer to the magnetic axis and the FWHM is narrower than the measurements. These differences are probably attributable to the zero-banana-width assumption in the current version of CQL3D code. Comparison with the finite banana-width treatment implemented in ORBIT-RF [36, 37] is in progress. In a future work, the combination of temporal, spectral and spatial resolution should allow for stringent tests of theoretical models of wave absorption.

Acknowledgments

References

[1] Ono M *et al* 2000 *Nucl. Fusion* **40** 557
[2] Kaye S *et al* 2005 *Nucl. Fusion* **45** S168
[3] Heidbrink W W and Sadler G J 1994 *Nucl. Fusion* **34** 535
[4] Fasoli A *et al* 2007 *Nucl. Fusion* **47** S264
[5] Kimura H, Fujii T, Saigusa M, Moriyama S, Hamamatsu K, Nemoto M and Tobita K 1993 *Plasma Phys. Control. Fusion* **35** 845
[6] Nemoto M, Kusama Y, Afanassiev V I, Hamamatsu K, Kimura H, Fujii T, Moriyama S and Saigusa M 1997 *Plasma Phys. Control. Fusion* **39** 1599
[7] Petty C C *et al* 1997 Fast wave current drive in neutral beam heated plasmas on DIII-D *Proc. 12th Int. Conf. on Radio Frequency Power in Plasmas (Savannah, GA, 1997))* (New York: AIP) p 225
[8] Eriksson L-G, Mantsinen M J, Rimini F G, Nguyen F, Gormezano C, Start D F H and Gondhalekar A 1998 *Nucl. Fusion* **38** 265
[9] Pinsker R I, Baity F W, Bernabei S N, Greenough N, Heidbrink W W, Mau T K, Petty C C, Porkolab M and the DIII-D Team 1999 Experiments on ion cyclotron damping at the deuterium fourth harmonic in DIII-D *Proc. 13th Int. Conf. on Radio Frequency Power in Plasmas (Annapolis, 1999)* (New York: AIP) p 144
[10] Heidbrink W W, Fredrickson E, Mau T K, Petty C C, Pinsker R I, Porkolab M and Rice B W 1999 *Nucl. Fusion* **39** 1369
[11] Petty C C *et al* 2001 *Plasma Phys. Control. Fusion* **43** 1747
[12] Mantsinen M J *et al* 2002 *Phys. Rev. Lett.* **88** 105002
[13] Noterdaeme J-M *et al* 2003 *Nucl. Fusion* **43** 202
[14] Rosenberg A L *et al* 2004 *Phys. Plasmas* **11** 2441

[15] Heidbrink W W, Luo Y, Burrell K H, Harvey R W, Pinsker R I and Ruskov E 2007 *Plasma Phys. Control. Fusion* **49** 1457

[16] Heidbrink W W, Burrell K H, Luo Y, Pablant N A and Ruskov E 2004 *Plasma Phys. Control. Fusion* **46** 1855

[17] Heidbrink W W, Bell R E, Luo Y and Solomon W 2006 *Rev. Sci. Instrum.* **77** 10F120

[18] Podestà M, Heidbrink W W, Bell R E and Feder R 2008 *Rev. Sci. Instrum.* **79** 10E521

[19] Harvey R W and Mccoy M G *1992 Proc. IAEA Technical Committee Meeting on Advances in Simulation and Modeling of Thermonuclear Plasmas (Montreal, Quebec, 1992)* (Vienna: IAEA)

[20] Medley S S and Roquemore A L 1998 *Rev. Sci. Instrum.* **69** 2651

[21] Medley S S and Roquemore A L 2004 *Rev. Sci. Instrum.* **75** 3625

[22] Shinohara K, Darrow D S, Roquemore A L, Medley S S and Cecil F E 2004 *Rev. Sci. Instrum.* **75** 3640

[23] Liu D, Heidbrink W W, Darrow D S, Roquemore A L, Medley S S and Shinohara K 2006 *Rev. Sci. Instrum.* **77** 10F113

[24] Luo Y, Heidbrink W W and Burrell K H 2004 *Rev. Sci. Instrum.* **75** 3468

[25] Luo Y, Heidbrink W W, Burrell K H, Kaplan D H and Gohil P 2007 *Rev. Sci. Instrum.* **78** 033505

[26] LeBlanc B P 2008 *Rev. Sci. Instrum.* **79** 10E737

[27] Bell R E *et al* 1998 *Princeton Plasma Physics Laboratory Report* PPPL-3591

[28] Levinton F M and Yuh H 2008 *Rev. Sci. Instrum.* **79** 10F522

[29] Heidbrink W, Miah M, Darrow D, LeBlanc B, Medley S, Roquemore A and Cecil F 2003 *Nucl. Fusion* **43** 883

[30] Hawryluk R J 1980 *An Empirical Approach to Tokamak Transport, in Physics of Plasmas Close to Thermonuclear Conditions* vol 1 (Brussels: CEC) pp 19–46

[31] Budny R V 1994 *Nucl. Fusion* **34** 1247

[32] Ongena J, Evrard M and McCune D 1998 *Trans. Fusion Technol.* **33** 181

[33] Kaita R, Goldston R, Beiersdorfer P, Herndon D, Hosea J, Hwang D Q, Jobes F, Meyerhofer D D and Wilson J R 1983 *Nucl. Fusion* **23** 1089

[34] Hawryluk R J *et al* 1991 *Plasma Phys. Control. Fusion* **33** 1509

[35] Kiptily V *et al* and J E contributors 2005 *Nucl. Fusion* **45** L21

[36] Chan V S, Chiu S C and Omelchenko Y A 2002 *Phys. Plasmas* **9** 501

[37] Choi M, Chan V, Pinsker R, Petty C, Chiu S, Wright J, Bonoli P and Porkolab M 2006 *Nucl. Fusion* **46** S409